Award Number: W81XWH-10-1-0713

TITLE: Magnetic Resonance Characterization of Axonal Response to Spinal Cord Injury

PRINCIPAL INVESTIGATOR: David B. Hackney, MD

CONTRACTING ORGANIZATION: Beth Israel Deaconess Medical Center
Boston, MA 02215-5491

REPORT DATE: December 2014

TYPE OF REPORT: Final

PREPARED FOR: U.S. Army Medical Research and Materiel Command
Fort Detrick, Maryland 21702-5012

DISTRIBUTION STATEMENT:

Approved for public release; distribution unlimited

REPORT DOCUMENTATION PAGE

Form Approved
OMB No. 0704-0188

1. REPORT DATE *(DD-MM-YYYY)*
December 2014

2. REPORT TYPE
Final

3. DATES COVERED *(From - To)*
27Sept2010 - 26Sept2014

4. TITLE AND SUBTITLE
Magnetic Resonance Characterization of Axonal Response to Spinal Cord Injury

5a. CONTRACT NUMBER

5b. GRANT NUMBER
W81XWH-10-1-0713

5c. PROGRAM ELEMENT NUMBER

6. AUTHOR(S)
David B. Hackney, MD

Email: dhackney@bidmc.harvard.edu

5d. PROJECT NUMBER

5e. TASK NUMBER

5f. WORK UNIT NUMBER

7. PERFORMING ORGANIZATION NAME(S) AND ADDRESS(ES)
Beth Israel Deaconess Medical Center
330 Brookline Avenue
Boston, MA 02215-5491

8. PERFORMING ORGANIZATION REPORT NUMBER

9. SPONSORING / MONITORING AGENCY NAME(S) AND ADDRESS(ES)
U.S. Army Medical Research and Material Command
Fort Detrick, Maryland 21702-5012

10. SPONSOR/MONITOR'S ACRONYM(S)
USAMRMC

11. SPONSOR/MONITOR'S REPORT NUMBER(S)

12. DISTRIBUTION / AVAILABILITY STATEMENT

Approved for public release; distribution unlimited

13. SUPPLEMENTARY NOTES

14. ABSTRACT

This work studied the ability to detect and characterize damage to spinal cord axons and myelin after spinal cord injury. Studies conducted at Beth Israel Deaconess Medical Center, the University of Pennsylvania and Drexel University produced promising results for assessing axon fiber diameter distributions in vivo. An initial focus on q-space imaging (QSI) was quantitatively successful in animal models and a STEAM based high b value approach was successfully implemented in human subjects. Direct myelin imaging was shown to be quantitatively reliable using ultra short TE (UTE) and zero TE (ZTE) methods in specimens. Myelin imaging in human subjects was implemented using inhomogeneous magnetization transfer (ihMT) methods. Overall, the results suggest that MR can detect and quantify these aspects of spinal cord damage after trauma. Further work will be required to adapt the laboratory methods to human imaging and to validate the quantitative results from the human methods pioneered here.

15. SUBJECT TERMS
Spinal Cord Injury, Magnetic Resonance Imaging, Q-Space Imaging, Ultra Short TE Imaging, Axonal Loss, Myelin

16. SECURITY CLASSIFICATION OF: Unclassified			**17. LIMITATION OF ABSTRACT**	**18. NUMBER OF PAGES**	**19a. NAME OF RESPONSIBLE PERSON** USAMRMC
a. REPORT U	**b. ABSTRACT** U	**c. THIS PAGE** U	UU	23	**19b. TELEPHONE NUMBER** *(include area code)*

Standard Form 298 (Rev. 8-98)
Prescribed by ANSI Std. Z39.18

Table of Contents

INTRODUCTION

Spinal cord injury can devastate lives, cause severe permanent disability, and early death. Although there are promising many avenues of investigation, a common challenge is determining the exact nature of the tissue damage sustained. The cord deteriorates after injury, and there are no reliable methods to predict the histological details. Yet, this information would be critical in selecting therapies and evaluating their effects on the intended targets. Limited success of a treatment could be due to applying it inappropriately. We seek to improve tissue characterization thus permitting better selection of potential therapy and better evaluation of treatment efficacy.

BODY

Overview

The overall goals of this project have been to use magnetic resonance (MR) of the spinal cord to infer damage to axons and to estimate myelin loss. We have made progress on these goals, with some limitations as described below.

A major goal has been to advance diffusion MR imaging of the cord. This involved improved technique for diffusion acquisition that would permit estimates of axonal density and diameter. An emerging approach for these studies has been q-space imaging (QSI). We have shown that this produces remarkably precise predictions of axonal diameter distributions when applied to fixed rat spinal cords and validated with microscopy. However, scaling this up to imaging live human subjects poses a number of technical problems that were a subject of our research. QSI typically relies on high q values, which are difficult to achieve in vivo. Part of our work focused on creating extremely high b value techniques that would permit direct assessment of axonal diameter as well as implementation of QSI.

We succeeded in obtaining high b value cross sectional imaging of human volunteer spinal cords and showed that these images reproduce reported axonal diameter distributions. Of course, we cannot directly validate these inferences with human subjects, as there are essentially no conditions what would require resection of the spinal cord to produce histological confirmation.

We have continued to pursue application to a human clinical imaging instrument. Our data continues to support the reliability of these estimates. This work thus encourages us to believe that we can use these insights to apply QSI to human subjects and derive valuable predictions of axonal density and diameter.

Another major goal has been inferring myelin loss after SCI. This is a prominent feature of injured cords. The loss of myelin severely impairs conduction velocity. Loss of oligodendrocytes also removes trophic support from the axons. Efforts at repair and regeneration involve, in part, attempts to restore normal spinal cord architecture, including remyelination. Currently there are no methods available to estimate myelin loss in human subjects. We have pursued two unrelated MR approaches to quantitating myelin.

The first directly visualizes myelin by creating images with extremely short TE values. These capture the short T2 signal of myelin, which is not detectable with conventional imaging. Using this approach, we have shown high quantitative accuracy in rat spinal cord specimens using a high field research instrument. Our goal of extending this work to human imaging has suffered technical and personnel problems as discussed below. We remain enthusiastic about the prospects for applying this work to human subjects, but substantial further technical development will be required.

The other approach to imaging spinal cord myelin has been applied in brain and spinal cord imaging in human subjects. This method relies on a feature of the magnetization transfer (MT) phenomenon. Specifically, it is possible to assess an asymmetry in MT, termed inhomogeneous magnetization transfer (IHMT) that appears unique to myelin. This approach has shown high association with known distribution of myelin and it appears to produce valuable estimates of myelin content. We have not, as of yet, validated the myelin estimates in animal models, but such studies are in the planning stages.

Thus, we have a method for myelin imaging that has shown high accuracy, validated in small animal spinal cord specimens and confirmed by biochemical determination of myelin content. This method will require substantial technical development to implement in human subjects, but if successful, it will permit direct visualization of in vivo myelin content. We have a second method that is readily performed in human subjects, but that awaits histological validation in animal models.

Between these two approaches, we believe we have made substantial progress on the second goal of assessing myelin content.

In depth summary of results

The original Statement of Work provided describes plans for three specific aims.

The first was to perform q-space MR imaging (QSI) and simulations of such imaging to determine the promise of this approach to describe axonal damage or integrity in spinal cord injury. The second aim was to develop several measures of myelin content in white matter. The third aim was to extend the methods developed in the first and second aims to normal volunteers and then to humans subjects with spinal cord injury.

The q-space work was severely hampered by equipment problems at the University of Pennsylvania where those studies were to be performed. After some initial successes further progress was limited.

The QSI studies extended our previous work establishing our ability to define the distribution of axon fiber diameters using this noninvasive approach. This work was presented at the Annual Meeting of the International Society of Magnetic Resonance in Medicine in Montreal, May, 2011 (Assessment of Axon Diameter Distribution in Mouse Spinal Cord with q-Space Imaging. Henry H. Ong1, Felix W. Wehrli) (Quantifying axon diameter and intra-cellular volume fraction in excised mouse spinal cord with q-space imaging. Ong HH, Wehrli FW.

Neuroimage. 2010 Jul 15;51(4):1360-6. doi: 10.1016/j.neuroimage.2010.03.063. Epub 2010 Mar 27. PMID: 20350604).

In addition, we made great progress with an ultra-short TE (UTE) method for myelin imaging. We have successfully implemented the ultra short TE (UTE) imaging approach to quantify myelin. Versions of this work were presented at Annual Meeting of the International Society of Magnetic Resonance in Medicine in Montreal, May, 2011, and at the Annual Meeting of the American Society of Neuroradiology in Seattle, June, 2011. This was published in the Proceedings of the National Academy of Sciences. The detailed data are provided in the paper, the following is a brief summary. Conventional MR imaging of the central nervous systems studies water protons exclusively. Although other compounds, such a lipid and proteins, have abundant protons the signal of these fades far too rapidly, due to their short T2, to permit detecting them with conventional techniques. Methods have been developed for identifying water protons whose behavior is closely enough linked to myelin that they permit estimates of myelin by viewing the myelin water fraction (MWF). This approach is promising, but since diseases that injure myelin also can alter water proton behavior, the MWF methods always face a confound on this basis. We have endeavored to image myelin lipid protons directly, rather than limit ourselves to myelin water. The extremely short T2 of myelin protons required implementation of an ultra-short TE (UTE) method that would detect these signals. Using this method we studied purified myelin preparations as well as excised rat spinal cord.

Below find a plot of the proton spectrum of a purified myelin suspension and rat spinal cord in D2O. Note that the spinal cord curve is a near perfect match for the “myelin” curve, derived from a protein-free suspension. Thus, the entire spinal cord white matter signal with this method derives from myelin lipid, and there is not a contribution from myelin protein. Although quantifying myelin protein might be useful, as a practical matter any method that relied on, or included signal from, protein would need to distinguish myelin from other proteins. Our results demonstrate that this method reports myelin lipid fraction alone, without the confound of myelin, or other, proteins.

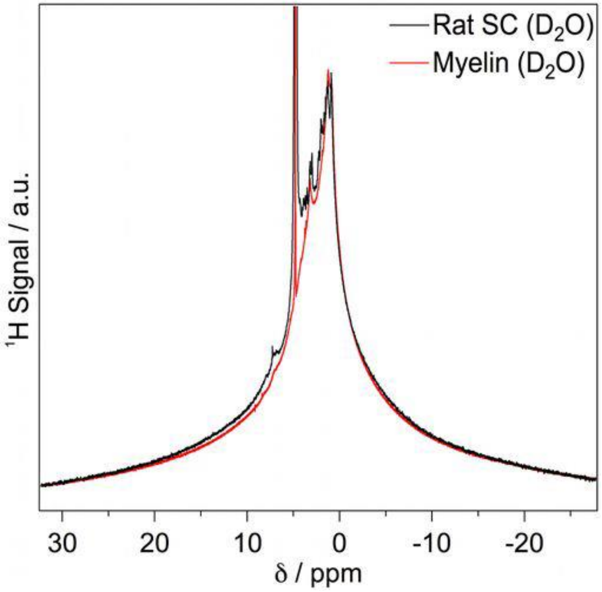

Figure 1: 1H NMR spectra of purified bovine myelin suspended in D2O (red) and D2O exchanged rat thoracic SC (black).

We have shown that the approach produces quantitatively reliable estimates of myelin content as assessed with graded concentrations of a D2O suspension of myelin lipid extract.

Figure 2a: The Figure displays fitted myelin peaks for myelin suspensions of graded concentrations

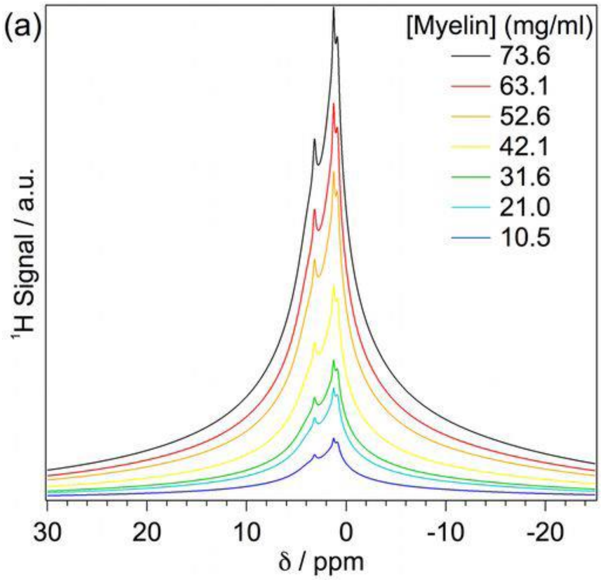

Based on these data, we determined the relationship between myelin signal intensity and known myelin concentration in suspension, finding a very high correlation (R2=0.99)

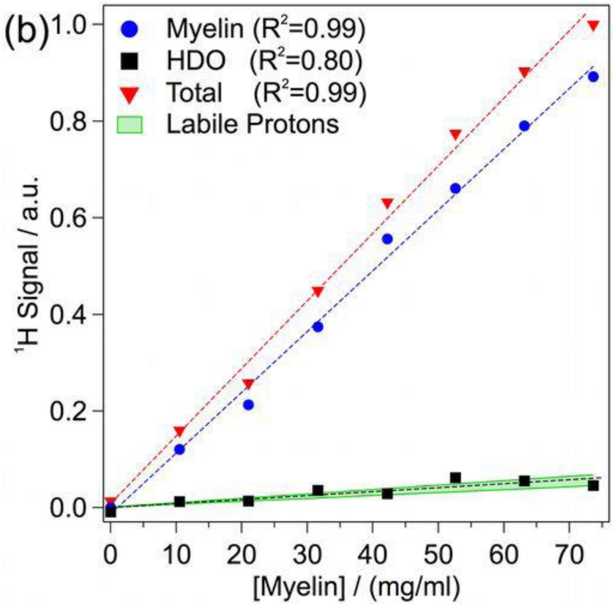

Figure 2b: Linear correlation plot of MR signal as a function of myelin concentration for the total (triangle), myelin (circle), and HDO (square) signal components.

This quantitative reliability of direct myelin imaging appears to be a novel finding in this field. This work was performed on normal cords to provide a starting point without the complications arising from spinal cord injury.

Using this approach we were able to establish quantitative accuracy vs. MR spectroscopy and preparations with known myelin content. This method holds promise for extension to human subjects, and it could offer a unique opportunity to observe myelin without confounding by other axonal injury or edema. This work initially was presented at the Annual Meeting of the International Society of Magnetic Resonance in Medicine in Montreal, May, 2011 (Prospects for Quantitative Imaging of Myelin with Dual-Echo Short Inversion Time 3D UTE MRI Michael J. Wilhelm, Henry H. Ong, Suzanne L. Wehrli, Ping-Huei Tsai1, David B. Hackney, Felix W. Wehrli) and a subsequent version was presented at the Annual Meeting of the American Society of Neuroradiology in Seattle, June, 2011. (Wilhelm, M. J., Ong, H. H.,Wehrli, S. L., Tsai, P., Wright, A. C., Hackney, D. B.,Wehrli, F. W. Prospects for Quantitative Imaging of Myelin with Ultrashort TE 3D Radial MR Imaging).The paper was published in the Proceedings of the National Academy of Sciences (Direct magnetic resonance detection of myelin and prospects for quantitative imaging of myelin density. Wilhelm MJ, Ong HH, Wehrli SL, Li C, Tsai PH, Hackney DB, Wehrli FW. Proc Natl Acad Sci U S A. 2012 Jun 12;109(24):9605-10. doi: 10.1073/pnas.1115107109. Epub 2012 May 24. PMID: 22628562

It was not possible to continue the QSI work due to the equipment failures at Penn and the spinal cord specimen imaging could not go forward without the MR instrument.

The second aim, developing methods for myelin content assessment in white matter was addressed with the direct myelin density work cited above. The application of inhomogeneous magnetization transfer for study of spinal cord white matter proved more challenging than anticipated and no publications arose during the term of the grant. However, Dr. Alsop and his collaborators did succeed in developing this method (Magnetization transfer from inhomogeneously broadened lines: A potential marker for myelin. Varma G, Duhamel G, de Bazelaire C, Alsop DC. Magn Reson Med. 2015 Feb;73(2):614-22. doi: 10.1002/mrm.25174. Epub 2014 Mar 6) and in generating spinal cord myelin maps (Magnetization transfer from inhomogeneously broadened lines (ihMT): Improved imaging strategy for spinal cord applications. Girard OM, Callot V, Prevost VH, Robert B, Taso M, Ribeiro G, Varma G, Rangwala N, Alsop DC, Duhamel G. Magn Reson Med. 2016 Mar 9. doi: 10.1002/mrm.26134. [Epub ahead of print])

The third aim, to extend quantitative imaging of spinal cord structure to human subjects succeeded for producing estimates of axonal integrity.

<u>In-vivo high resolution high b-value diffusion imaging of the spinal cord.</u>

Axon fiber structure inferences derive from diffusion imaging of the spinal cord. The major challenges for human in-vivo diffusion imaging arise from the cord’s small size, motion, and variations in magnetic susceptibility surrounding the spine that require reduced field of view approaches. Limited diffusion sensitivity (b-values) until now has prevented reliable detection of variations in axon diameter in vivo. In this work, we have pioneered an approach to obtaining very high b values for in vivo imaging and demonstrated sensitivity to axon fiber architecture in cross sectional imaging of the cord.

Methods

Pulse Sequence

All experiments were performed on a 3.0 T GE Signa HDx scanner (GE HealthCare, Waukesha, WI, USA) with maximum gradient strength of 40 mT/m and a maximum achievable slew rate of 150 T/m/s. An EPI sequence capable of diffusion-weighted (DW) imaging using twice-refocused spin echo (TRSE) was modified for a stimulated echo acquisition mode (STEAM) excitation. The spatial-spectral pulse that forms the first RF excitation pulse in the sequence was retained. The second and third 90° RF excitation pulses were modified from 180° in the TRSE sequence in the STEAM sequence, and occurred concurrently with slice selection gradients. With this change, the echo time (TE) was now the sum of the duration between the first and second RF pulses and the duration between the third RF pulse and the central k-space line in image acquisition.

Diffusion-weighting gradients were applied right before the second RF pulse and right after the third RF pulse. The mixing time (TM), defined as the duration between second and third RF pulses, was user-selectable with a maximum possible value of 2 seconds. Crushers designed to cause dephasing of up to 8π radians were placed within the mixing period to retain only the longitudinal magnetization. This modified pulse sequence allowed the acquisition of DW images with b of up to ~31,000 s/mm2 when the diffusion time (□) = 2 s. The lower TE used by the STEAM sequence facilitated the use of longer TMs and, thus, longer diffusion times, with limited impact of signal decay due to T2* relaxation.

Data Acquisition

The STEAM DW imaging sequence was used to acquire axial images of the cervical spinal cord (C4-C5) in six healthy volunteers (3 female, age = 18 – 32 years), using an eight-channel cervical-thoracic-lumbar (CTL) phased-array RF receive coil, with the first three channels activated. In the first experiment, a range of twelve linearly-spaced b’s was selected with diffusion gradients placed in the right-to-left direction and maximum b-value of 1100 s/mm2 for each Δ = 76, 130, 230, 490, and 1000 ms. This data will be referred to as ‘b1100’ in the following text. The following imaging parameters were used: TR = 2500 – 4000 ms, TE = 42-60 ms, FOV = 12 cm, acquisition matrix = 96 frequency encodes × 48 phase-encoding steps, left-to-right frequency direction, phase FOV = 0.5, slice thickness = 10 mm. Spatial saturation bands were placed anterior and posterior to the slice of interest to allow the acquisition of a reduced FOV. All images were reconstructed to form 128 × 128 matrices.

In the second experiment, only TM was progressively increased to increase the maximum b-value as diffusion time Δ increased, while keeping all other diffusion-related parameters the same across Δs. For each Δ = 250, 500, and 1000 ms, twelve images with diffusion sensitization perpendicular to the spinal cord, in the right-to-left direction, were acquired with the DW STEAM EPI pulse sequence, and the following imaging parameters: TR = 2500 – 4000 ms, TE = 60 ms, FOV = 12 cm, acquisition matrix = 96 frequency encodes × 48 phase-encoding steps (reconstructed matrices of 128 × 128), left-to-right frequency direction, phase FOV = 0.5, slice thickness = 10 mm, with spatial saturation bands placed anterior and posterior to the slice and diffusion sensitization in the right-to-left direction. The maximum possible b-values corresponding to increasing Δ were 3650, 7400, and 15000 s/mm2, with increased spacing between the higher b-values. This data will be referred to as the ‘bmax’ or ‘full’ dataset in the following text.

Raw data were saved for all acquisitions, along with reference data used for EPI phase correction of Nyquist ghosts and correction matrices used to accommodate k-space points sampled on the gradient ramps.

Post-Processing

Tools for image reconstruction and post-processing were developed in-house using MATLAB (The MathWorks, Natick, MA, USA). Raw k-space data corresponding to each image were first corrected for variable-gradient sampling of k-space, followed by phase correction for constant and linear phase errors using the reference data acquired from a non-phase encoded acquisition and obtainable on the MRI scanner. Next, the low-pass Fermi filter, given by $H(i,j)= 1/(1+\exp((k(i,j)-B)/A))$ with A = 0.05 and B = 0.8, was used to smooth k-space, followed by iterative Homodyne processing. All of these operations were carried out on individual excitations and receiver channel outputs. At this stage, the low-resolution (48×96) images were averaged across excitations. It was found that only one receiver channel contained most of the signal, and so the contributions from the other receiver channels were discarded. The final step involved interpolation to 64×128 matrices, yielding one image corresponding to each combination of b-value and diffusion time Δ.

Each set of images (with the same Δ and a range of twelve b-values) was processed separately. Post-processing began with a noise-floor reduction step, in which the noise was estimated by calculating the mean of the signal from a region of interest (ROI, 100 pixels) placed in the background on the five images weighted with the highest b-values. This number was subtracted from the entire set of twelve images to reduce the noise floor. Next, one ROI was chosen for each set of diffusion-weighted images, (a) to encompass the entire spinal cord (an ROI of ~80 pixels, i.e., ~700 mm3 voxel), (b) to select only gray matter (GM, with an ROI of 8 pixels, i.e., a 70.3 mm3 voxel) within the anterior columns, and (c) to select only white matter (WM, with an ROI of 8 pixels, i.e., a 70.3 mm3 voxel) within the posterior funiculus.

For each volunteer, the signal decay curves obtained from the selected ROIs for a combination of b and Δ were input to several fitting equations using a non-linear least-squares algorithm, including:

- The mono-exponential (ME) signal decay model, given by $S_b=S_0 e^{-b.ADC}$, where Sb is the signal within the ROI at a given b-value (b), S0 is the signal at b ~ 0 s/mm2, ADC is the apparent diffusion coefficient (ADC). Boundary conditions for the ADC were set at [10-8 -10-1].
- A bi-exponential (BE) signal decay model was employed, given by $S_b= S_0 (fe^{-b ADC_f}+(1-f) e^{-b ADC_s})$, where Sb is the signal within the ROI at a given b-value (b), S0 is the signal at b ~ 0 s/mm2, ADCf and ADCs are the ADCs of the fast and slowly decaying components, respectively, where the fraction of the fast-decaying

component is denoted by f. Boundary conditions for f, ADCf, and ADCs were set at [0 1], [10-6 10-1], and [10-8 10-2], respectively.

- The diffusional kurtosis (DK) decay model was employed, given by S_b= S_0 (e^(-b.ADC+ K_app/6 〖(b.ADC)〗^2)) , where Sb is the signal within the ROI at a given b-value (b), S0 is the DK signal at b ~ 0 s/mm2, ADC is the apparent diffusion coefficient (ADC), and Kapp is the excess kurtosis of the diffusion displacement probability function. Boundary conditions for Kapp and ADC were set at [0 10] and [0 1], respectively.

The stopping criterion for the three models was set to a residual error of 10-12 or less. All models were implemented with MATLAB's optimization toolbox, and S0 was also an unknown in each case.

Results

Figure 3 shows example images acquired in vivo using the diffusion-weighted STEAM pulse sequence on one volunteer, with b ~ 550 s/mm2 (top row) and the highest possible b-value (bmax, bottom row) for Δ = 76 ms (first column, with bmax ~ 1100 s/mm2), 250 ms (second column, with bmax ~ 3650 s/mm2), 500 ms (third column, with bmax ~ 7350 s/mm2), and 1000 ms (fourth column, with bmax ~ 14750 s/mm2). All images were reconstructed from the raw data files and are shown with identical window and level settings. As seen from the images with b ~ 550 s/mm2, the lower signal to noise ratio (SNR) is due to increasing TMs, but the diffusion images are visually consistent, even at the longest diffusion time of one second. The images in the right column were acquired with increasing Δ and b, clearly showing increasing contrast between the anterior columns of gray matter and the surrounding white matter. It is also remarkable that enough signal is preserved even with Δ = 1000 ms and a large diffusion weighting factor of b ~ 14750 s/mm2. In this image, it is also possible to indicate the pixels containing the posterior columns of gray matter surrounding the posterior funiculus of white matter.

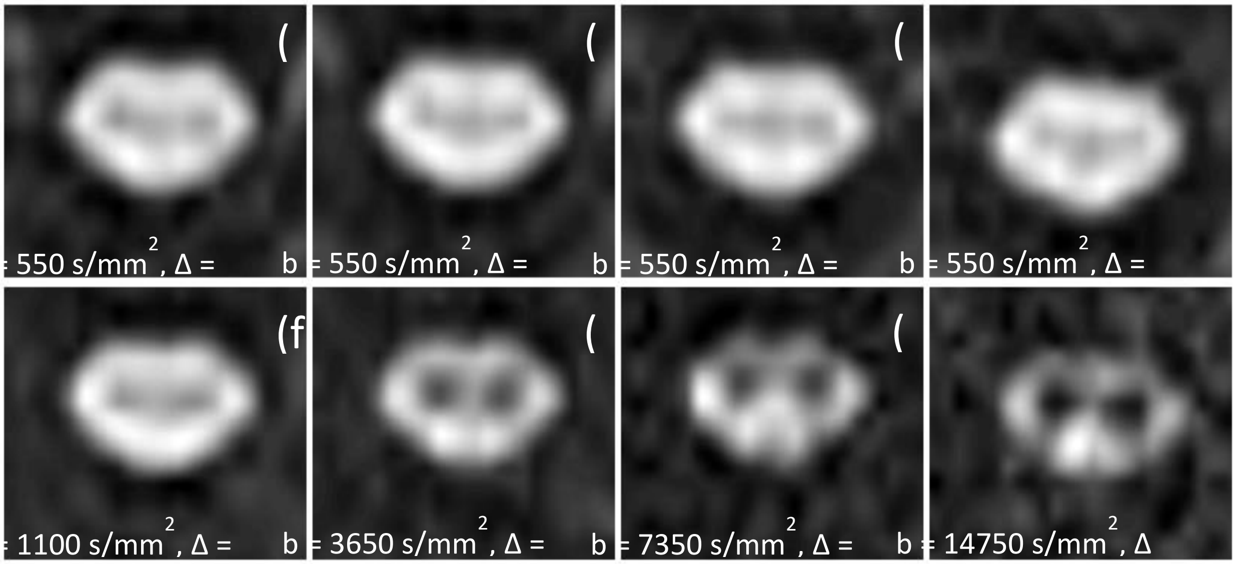

FIG 3: DW-STEAM images with b = 550 s/mm2 (top row) and maximum possible b-values (bottom row) for diffusion times (Δ) of 76 ms (first column), 230-250 ms (second column), 490-500 ms (third column), and 1000 ms (fourth column). Window and level settings were adjusted independently for each image.

In order to compare the fitting results across a range of b-values larger than that used in the first experiment and to ascertain if the variations in fitting parameters were a function of Δ, the ROI analysis was performed on a subset of the data obtained from the second experiment. Specifically, the signal decay curves corresponding to the entire cord and with b = 0 ~ 3500 s/mm2 for diffusion times from 250 ms to 1000 ms were input to the fitting routines. This resulted in 12, 8, and 5 points for Δ = 250, 500, and 1000 ms, respectively. This data will be referred to as the ‘b3500’ or ‘truncated’ dataset in the following text. As before, the truncated signal decay curves were fit to the ME, BE, and DK equations, and fitting parameters obtained were averaged across volunteers for comparison with the datasets using the full range of b.

Two-tailed pairwise statistical significance tests were performed to compare fitting parameters (a) across Δ = 250 – 1000 ms for the truncated (b3500) datasets, and (b) between WM and GM over Δ = 250 – 1000 ms, for the full and truncated datasets.

With the exception of one series of images acquired on one volunteer with Δ = 490 ms and bmax = 1100 s/mm2, all data from all six volunteers was used for further analysis. Of the three fitting equations, the BE fit yielded inconsistent parameters with large inter-subject variations when applied to ROIs comprising the entire cord, the WM and the GM, and was therefore excluded from further discussion.

Mono-exponential and diffusional kurtosis fitting equations introduced earlier were applied to the data acquired in experiment 1 (i.e., with bmax ~ 1100 s/mm2). For the ROI comprising the entire cord, the ME fit yields a consistent ADC of 5.66 × 10-4 mm2/s over all volunteers, for Δ = 76 = 1000 ms. WM ADC was 3.7 × 10-4 mm2/s, while GM ADC was 5.49 × 10-4 mm2/s. The DK fit yielded average ADCs of 6.85 × 10-4 mm2/2 with Kapp of 1.26 ± 0.38 over the range of Δ with large inter-subject variation of Kapp in data acquired within a single diffusion time, indicating lower consistency over this range of b-values. WM and GM ADC values were 4.79 × 10-4 mm2/s and 6.91 × 10-4 mm2/s, respectively, for the DK fit. Kapp was 2.05 ± 0.35 for WM and 1.18 ± 0.59 for GM across Δ with large variability across subjects within a single Δ.

Data in experiment 2 was acquired by concurrently increasing both the range of b-values and diffusion time. Previous studies have shown that the ME fit is inadequate to explain signal decay with large b-ranges, leading to underestimation of ADC. The same was observed with this data, as ADC decreased from 4.1 × 10-4 mm2/s at Δ = 250 ms to 1.6 × 10-4 mm2/s at Δ = 1000 ms, for the ROI comprising the entire cord. Similarly, the DK fit showed ADCs from 6.3 × 10-4 mm2/s at Δ = 250 ms decreasing to 3.0 × 10-4 mm2/s at Δ = 1000 ms, and Kapp decreasing from ~1.2 at Δ = 250 ms to ~0.9 at Δ = 1000 ms. Figure 2a is an example illustrating the use of the DK signal decay equation to fit the bmax data on one volunteer. The data points acquired using each Δ were normalized to their corresponding S0 obtained using the ME equation on the signal attenuation curve of up to b ~ 1750 s/mm2 for comparison on the same scale. This figure shows that the signal decay curve can be well approximated by the DK equation by a range of b-values extending only up to ~ 3000 s/mm2.

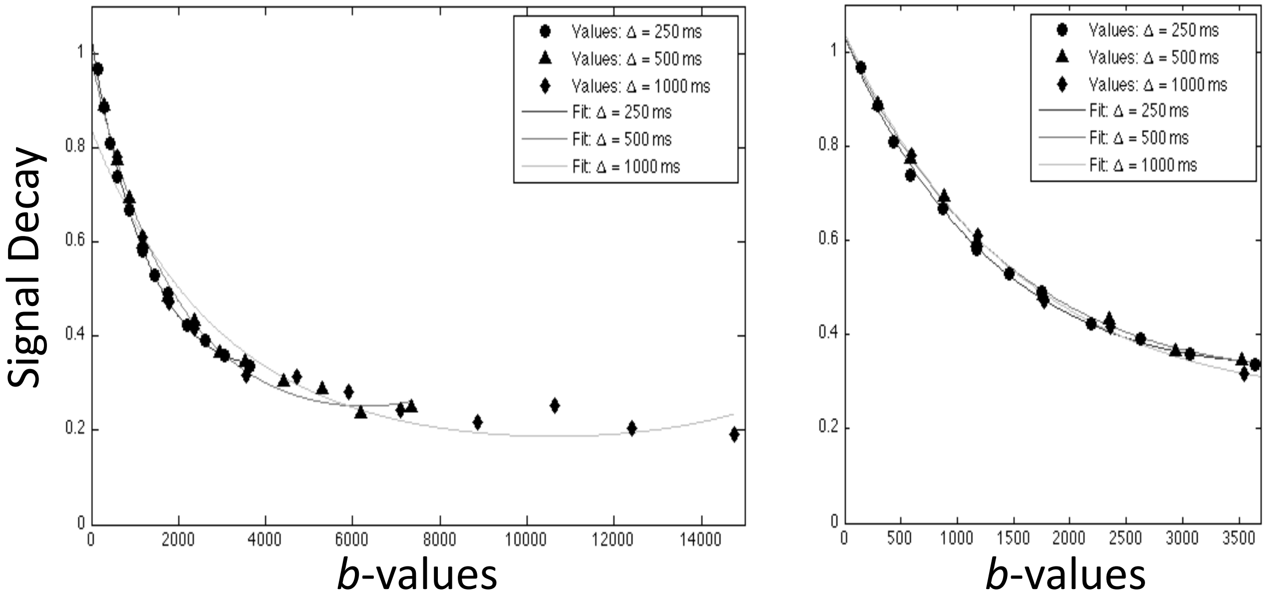

FIG 4: Data points (markers) and fitting results (solid lines) using the DK signal decay equation on ROIs comprising the whole cord, with (a) the full range of b-values of up to 15000 s/mm2, and (b) with the truncated range of b-values of up to 3650 s/mm2, for Δ = 250 – 1000 ms. Data acquired with each Δ were normalized to the corresponding S0 obtained using the ME equation on the signal attenuation curve of up to b ~ 1750 s/mm2 for comparison across Δ and b-values, and are shown for one volunteer only.

Applying the fitting algorithms to smaller ROIs obtained from WM and GM highlighted the differences between these tissue types, especially as the Δ and corresponding b-value range increased. For example, the ADCs obtained in the ME fit decreased from 2.73 × 10-4 mm2/s at Δ = 250 ms to 0.62 × 10-4 mm2/s at Δ = 1000 ms in WM, and from 4.71 × 10-4 mm2/s at Δ = 250 ms to 3.14 × 10-4 mm2/s at Δ = 1000 ms in GM. Similarly, ADCs in the DK fit decreased from 4.23 × 10-4 mm2/s to 1.3 × 10-4 mm2/s in WM and from 6.7 × 10-4 mm2/s to 4.5 × 10-4 mm2/s in GM (Figure 5a). Average values of kurtosis in WM were 1.4 ~ 1.8 and found to remain consistent across Δ with large inter-subject variability in WM, while decreasing across Δ from 1.03 to 0.57 in GM (Fig. 5b). In general, the fitting parameters exhibited lower inter-subject standard deviation with increasing Δ and b-ranges. There were statistically significant differences between GM and WM parameters, with p-values increasing as the range of b-values increased.

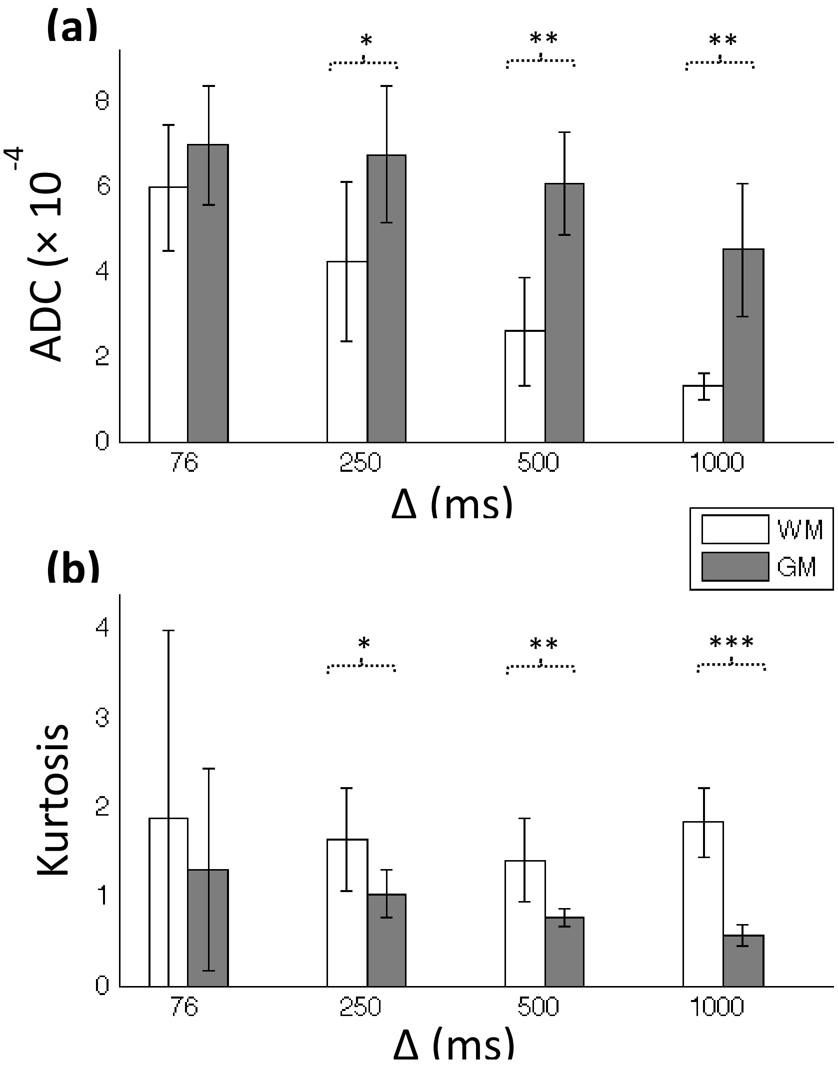

FIG 5: (a) shows ADC value, and (b) shows kurtosis values obtained with DK fit applied to signal decay with b-values of up to 15000 s/mm^2 in WM (first column, white bar) and GM (second column, gray bar). P-values (* - $p < 0.05$, ** - $p < 0.01$, *** - $p < 0.001$) indicate significant differences between WM and GM with increasing *b*-value range. Error bars are the standard deviations in parameters across subjects.

FIG 5: (a) shows ADC value, and (b) shows kurtosis values obtained with DK fit applied to signal decay with b-values of up to 15000 s/mm2 in WM (first column, white bar) and GM (second column, gray bar). P-values (* - $p < 0.05$, ** - $p < 0.01$, *** - $p < 0.001$) indicate significant differences between WM and GM with increasing b-value range. Error bars are the standard deviations in parameters across subjects.

In general, the results of the first experiment indicate the need for a larger range of b-values to obtain consistent fitting parameters, while the results of the second experiment suggest that increasing b-ranges with increasing diffusion times may result in significantly different parameters. The third analysis was performed on a large and consistent range of b-values up to 3500 s/mm2 for all diffusion times Δ = 250 – 1000 ms (Fig. 4b). Fitting the signal decay using the large ROIs showed less change in ADC, i.e., from 4.1 × 10-4 mm2/s at Δ = 250 ms to 3.3 × 10-4 mm2/s × 10-4 mm2/s at Δ = 1000 ms using ME, and from 6.2 × 10-4 mm2/s at Δ = 250 ms to 5.1 × 10-4 mm2/s at Δ = 1000 ms in DK, with kurtosis constant at ~1.15 (Figure 6). No significant difference in the fitting parameters was found over the range of diffusion times investigated in this study.

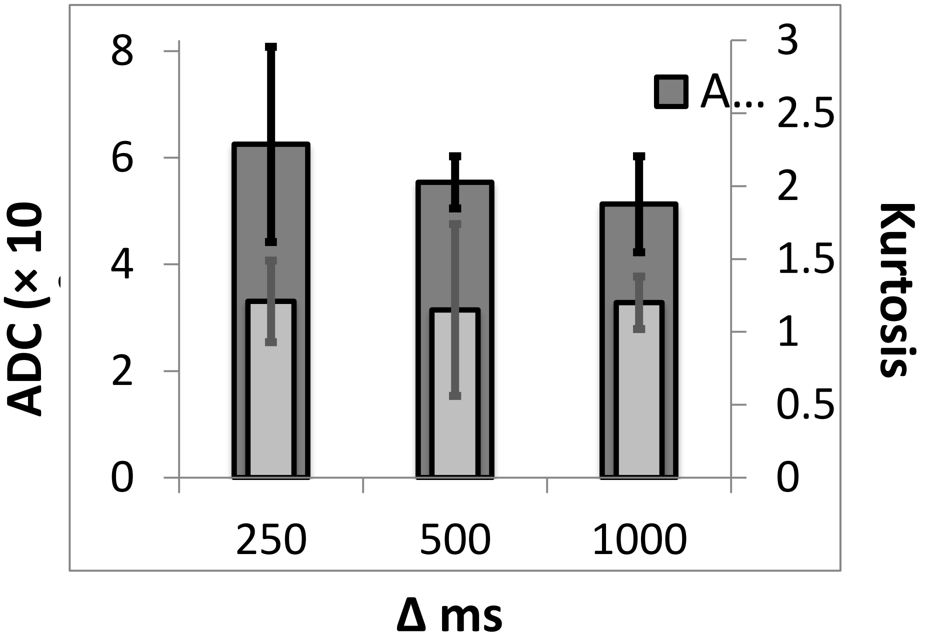

Figure 6 shows ADC (dark gray) and kurtosis (light gray) obtained with DK fit applied to signal decay with b-values of up to 3500 s/mm2 in an ROI comprising the entire cord. P-values do not indicate any significant differences when compared pair-wise across diffusion time when the same range of b-values is used to fit the signal attenuation curves. Error bars show inter-subject standard deviations.

WM and GM ROI analyses using the ME fit over the truncated b-value range yielded WM ADCs of 2.7 × 10-4 mm2/s for Δ = 250 ms, decreasing to 1.6 × 10-4 mm2/s for Δ = 1000 ms. GM ADC remained nearly constant at 4.63 × 10-4 mm2/s across the range of diffusion times. The DK fit yielded WM ADCs of 4.23 × 10-4 mm2/s at Δ = 250 ms to 2 × 10-4 mm2/s at Δ = 1000 ms for WM, with GM ADC of ~ 7 × 10-4 mm2/s over the range of Δ. Similarly, kurtosis of GM stayed approximately constant at 0.92, however kurtosis of WM exhibited large variations across subjects and over Δ, with no consistent trend visible. WM ADC values for the ME and DK fits were significantly different in the pair of Δ = 250 ms and Δ = 1000 ms, however kurtosis showed no significant differences across diffusion times. None of the GM parameters was significantly different across diffusion times.

These results are notable for several reasons. They highlight the difficulty of monoexponential fits in accurately reflecting the diffusion properties of the spinal cord, particularly when data is obtained with a wide range of b values. This has important technical implications for interpretation of diffusion data, extraction of fractional anisotropy, kurtosis, and other higher order parameters from diffusion data. Since higher b value imaging emphasizes slower-diffusing components, this reveals cord structure not previously visible with in vivo MR techniques. Perhaps most readily applicable to human spinal cord injury, the results in Figure 1 demonstrate changing contrast across the white matter at higher b values. The dorsal columns and lateral corticospinal tracts have progressively relative preserved signal as the b values increase. This differential effect has not been previously reported in humans in vivo, although it was expected based on the known axonal architecture of the cord. These are regions of higher axonal density and consequently, smaller diffusion barrier spacing. This information is similar to that sought in q-space studies. However, this contrast is now observed directly from our acquired images, rather than extracted from, often noisy, q-space experiments.

Myelin imaging with ihMT.

We implemented in inhomogeneous magnetization transfer (ihMT) method to detect myelin in spinal cord white matter. Previous approaches to estimating myelin content have relied on diffusion imaging, with problematic interpretation as reflecting myelin alone. Conventional magnetization transfer techniques are confounded by other effects that are commonly seen in CNS injury, including high sensitivity to edema. Thus, MT alone cannot reveal myelin content in the setting of spinal cord injury.

Conventional magnetization transfer (MT) imaging has been explored as a potentially sensitive marker to myelin in neurological disorders. However, MT is not a specific marker of white matter damage due to demyelination. We recently reported a technique to extract the ‘inhomogeneous’ component of MT (ihMT), which was shown to be specific to myelin in brain. The ihMT component is thought to come from more mobile macromolecular pools that cause asymmetrical line broadening about the center frequency, and can be extracted by applying MT saturation pulses with alternating (positive/negative) off-resonance frequencies. The goal of this study was to use the ihMT imaging technique to acquire a global myelin-specific image over the cervical spinal cord in the sagittal plane. A myelin-specific MT imaging technique may accurately and specifically reflect axonal damage in the event of spinal cord injury.

<u>Methods:</u> Images were acquired on a 3.0 T scanner (GE Healthcare, Waukesha, WI) using the upper half of a twelve-channel spine receiving coil. Inhomogeneous MT images were acquired by applying a pulsed saturation scheme for 500 ms, consisting of 500 μs Hanning-shaped pulses applied every 1.5 ms with a +/- 7.0 kHz frequency offset to acquire four images in each set, as follows: positive frequency offset (A), alternating dual frequency offset (B), negative frequency offset (C), alternating dual frequency offset (D). The average power of the MT pulses was 35 mG. Following the saturation, a single slice was acquired using single-shot spin-echo echo planar imaging (EPI) in the sagittal plane comprising the brainstem and cervical spinal cord, with the following imaging parameters: TR/TE = 2500/23 ms, FOV = 18 cm, phase FOV = 0.5, acquisition matrix 96 × 48 (reconstructed to 128 × 64), slice thickness = 10 mm, with 54 averages of each set and an additional eight averages of the unsaturated EPI image, for a total

scan duration of ~ 9 minutes. This protocol was followed on two healthy volunteers (female, 32 and 37 years).

The images were combined to yield the ihMT component image, given by: ihMT = (A + C) – (B + D). Inhomogeneous MT ratios (ihMTR) were calculated by normalizing the ihMT images by the unsaturated EPI images. For comparison, the MT ratio (MTR) was also calculated using image ‘A’ as the saturated image. A mask was applied to select only the brainstem and spinal cord, and was used to calculate ihMTR as a function of position along these regions. Results: Figure 7 demonstrates the result of this experiment on one volunteer. The unsaturated EPI image is shown in Fig. 7a, Fig. 7b shows the MT ratio, and the ihMT ratio is shown in Fig. 7c, clearly illustrating the specificity of this measure to myelin. The variation in ihMTR along the long axis of the cord and into the brainstem (Fig. 7d) is likely at least in part a function of partial volume effects. In the future, we propose to address this with a combination of careful alignment of the imaging axis along the long axis of the spinal cord, and use of thicker sections. Since only the WM appears to demonstrate this ihMT effect, inclusion of adjacent CSF will not influence the results. Here the MT effect arises not only from the saturation of other macromolecules along with myelin in the cord but also from direct saturation effects. Similar results were seen on the second volunteer.

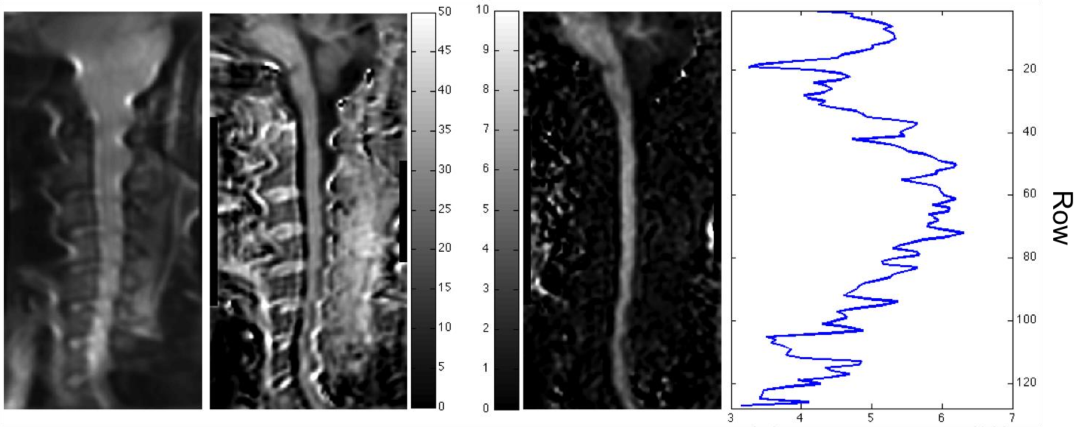

(a) EPI (b) MTR image (%) (c) ihMTR image (%) (d) ihMTR in cord (%)

FIGURE 7 shows (a) unsaturated EPI, (b) MTR, and (c) the inhomogeneous MTR. Note the specificity of the ihMTR image to white matter in the cerebellum (the arbor vitae can be seen), brainstem, and cervical spinal cord. The ihMTR is shown as a function of its location along the brainstem and cord (not including the cerebellar white matter) in (d).

Inhomogeneous MT imaging is clearly sensitive to regions within the cerebellum, brainstem, and cervical spinal cord. Its specificity to myelin in white matter is evidenced by the absence of signal in cerebellar gray matter, vertebrae, intervertebral disks, subcutaneous fat, and cerebrospinal fluid. Signal differences in ihMT between the spinal cord and the brainstem (particularly the medulla oblongata) are expected due to fractional differences in white matter between these regions. Although several averages were acquired to improve the signal to noise ratio (SNR), the ihMT quantification remained the same even with 1/4th the number of averages (data not shown). This, along with the consistency of the values in two volunteers, indicates the robustness of the measure.

Human subjects studied and demographics

A total of 42 subjects were consented for imaging under the IRB's for this work.

As discussed elsewhere in the report, we did not get the clinical imaging to the point that we wanted to burden patients with spinal cord injuries with coming to BIDMC and getting on the scanner. The methods were developed and implemented primarily for the cervical spinal cord, which has a larger cross section and combination of large areas of grey matter and white matter. This works well for normal subjects and some technical details of MR imaging work best in the cervical region. However, it also poses challenges for imaging patients with spinal cord injury. Due to the level of injury, these patients often have arm weakness as well as leg weakness and many have associated problems with airway and breathing that make lying motionless on their backs for extended periods quite difficult. Although we believe these methods will come to fruition for thoracic cord injuries and that more rapid approaches will make it practical to study patients with cervical lesions, we did not get to the point that we thought it was appropriate to study such patients. Scanning patients with cervical cord injuries requires considerable effort on their part to come into town and to get on the MR table. Since the clinical imaging remained developmental, we used the availability of normal subjects to perform sometimes quite prolonged imaging studies. Therefore, all the subjects were normal volunteers.

Of the 42 who consented, 40 subjects successfully completed the imaging session.

Gender:
16 Males
26 Females

Race:
Multi-racial: 2
Decline to answer: 2
Asian: 7
Other: 2
White: 29

Age, race and ethnicity

Age	**M/F**	**Latino/ Hispanic?**	**Race**
26	F	N	White
23	F	N	White
31	M	N	White
31	F	N	Multi-racial
28	M	Decline	Decline
20	M	N	White
28	M	N	White
25	F	N	White

26	F	N	White
26	F	N	White
48	M	N	White
32	F	N	Asian
29	M	Decline	Decline
32	F	N	Asian
32	F	N	Asian
48	M	N	White
22	F	N	White
32	F	N	Asian
29	M	N	Asian
37	F	N	Asian
22	F	N	White
30	F	N	White
22	F	N	White
29	M	N	White
32	F	N	Other
37	F	N	Asian
22	F	N	White
29	M	N	Other
24	F	N	White
23	F	N	White
23	F	N	White
27	M	N	White
23	M	N	White
53	M	N	White
32	M	N	White
29	F	N	White
25	F	N	White
28	M	N	White
23	F	N	White
22	M	Y	White
23	F	N	Multi-racial
23	F	N	White

Limitations: The University of Pennsylvania site has been hampered by equipment problems. An upgrade of the high field MR imaging equipment, which ultimately will improve the capabilities of the instrument, created major delays. The new scanner required completely new pulse sequences and hardware upgrades to restore the ability to use a custom-built gradient coil. This coil, designed and fabricated in-house, permitted far higher imaging resolution and gradient stability that off the shelf alternatives. However, the incompatibility of the coil and software with the new instrument introduced severe delays in completing the goals of the high field imaging of small animal spinal cords- a key feature of the work at UPenn. Therefore, we could not perform the planned imaging of spinal cord injured specimens generated at Drexel.

The Beth Israel Deaconess Medical Center (BIDMC) site also experienced delays, in this case due to personnel turnover. A postdoctoral fellow who worked quite productively on the IHMT and high b-value imaging left due to family reasons, creating major delays in carrying with work forward. However, both components of the project showed substantial progress.

The work described here was successful in several measures. The application was extremely ambitious and some of the areas were mired in technical development that was far more time consuming than anticipated.

The QSI work established that the method could report a distribution of axon fiber diameters, shown to be reliable in animal models. Extension to human subjects imaging has been attempted by others with variable success. Of course, in these subjects the accuracy of predicted diameters cannot be evaluated, but the studies are hampered by the q resolution obtainable with clinical imaging equipment. This area remains promising for application to normal subjects and to patients. However, the shift of fiber diameters to smaller axons preserved after spinal cord injury will remain a challenge for this method.

The UTE approach for direct myelin quantitation is also promising and shown to be reliable in specimens. Moving this to human subjects will be a major undertaking as the methods are currently beyond the capabilities of clinical MR instruments.

The ihMT approach to estimating myelin content has been applied in humans, first in brain and later in spinal cord. This approach, while remaining technically challenging, faces fewer obstacles than the QSI or UTE methods. The major limitation, besides implementation, is the less certain interpretation of the results as truly reflecting myelin. There are excellent observational data supporting this understanding of the phenomenon and theoretical reasons why myelin should have the effects seen. It is less certain that myelin is the only tissue element that could produce ihMT, particularly in injured cords. It is also not yet clear how much myelin must be damaged or lost to reduce or eliminate the ihMT effect. Thus, this method does not yet provide quantitative estimates of myelin integrity or content.

Because of the technical challenges outlined above, we did not to progress to the point that we felt it appropriate to study spinal cord injured patients. For such patients, the trip to BIDMC for imaging and the difficulty of getting on the MR instrument would have required more progress in implementing these methods in vivo in normal volunteers first.

KEY RESEARCH ACCOMPLISHMENTS

- Implemented animal models of spinal cord injury.
- Demonstrated direct imaging of myelin using ultra short TE and zero TE techniques.
- Demonstrated the quantitative accuracy of these myelin measures.
- Performed QSI on small animal spinal cord specimens.
- Generated preliminary data on QSI imaging on a human clinical MR instrument.

- Implemented upgrades to the Bruker small bore high field MR instrument permitting use of a custom built spinal cord coil.
- Developed high b-value imaging of the human spinal cord in volunteers.
- Demonstrated axonal diameter distribution correlates of cross sectional imaging in human spinal cord in vivo.
- Applied IHMT to spinal cord imaging in human subjects.
- Documented high IHMT in spinal cord white matter, correlating with myelin content and low values in grey matter.
- High spatial resolution spinal cord QSI for estimation of axonal diameter distribution.
- Quantitative direct myelin imaging in spinal cord.
- High b-value spinal cord imaging in human subjects correlates with axonal diameters.
- IHMT imaging in human subjects correlates with myelin content.

REPORTABLE OUTCOMES Manuscripts published

Wilhelm, M; Ong, H; Wehrli, S; Li, C; Ping-Huel, T; Hackney, D; Wehrli F. Direct magnetic resonance detection of myelin and prospects for quantitative imaging of myelin density. PNAS. 2012, 109, 24:9605-9610.

Rangwala, N; Hackney, DB; Dai, W; Alsop, D. Diffusion restriction in the human spinal cord characterized in vivo with high b-value STEAM diffusion imaging. Neuroimage. 2013. 82: 416-425.

Conference presentations

Assessment of Axon Diameter Distribution in Mouse Spinal Cord with q-Space Imaging. Henry H. Ong, Felix W. Wehrli) (Quantifying axon diameter and intra-cellular volume fraction in excised mouse spinal cord with q-space imaging. Ong HH, Wehrli FW. 19th Annual Meeting and Exhibition, International Society of Magnetic Resonance in Medicine, Montreal, Canada, May, 2011.

Wilhelm, M. J., Ong, H. H.,Wehrli, S. L., Tsai, P., Wright, A. C., Hackney, D. B.,Wehrli, F. W. Prospects for Quantitative Imaging of Myelin with Ultrashort TE 3D Radial MR Imaging. 49th Annual Meeting of the American Society of Neuroradiology, Seattle, WA, June, 2011.

Prospects for Quantitative Imaging of Myelin with Dual-Echo Short Inversion Time 3D UTE MRI Michael J. Wilhelm, Henry H. Ong, Suzanne L. Wehrli, Ping-Huei Tsai1, David B. Hackney, Felix W. Wehrli. 21st Annual Meeting and Exhibition, International Society of Magnetic Resonance in Medicine, Salt Lake City, UT, April, 2013.

Quantification of Myelin in the Cervical Spinal Cord Using Inhomogeneous Magnetization Transfer Imaging. Novena Rangwala1, Gopal Varma1, David Hackney1, David C. Alsop. 21st Annual Meeting and Exhibition, International Society of Magnetic Resonance in Medicine, Salt Lake City, UT, April, 2013.

High b-Value Diffusion-Weighted Imaging on Human Spinal Cord in Vivo: Investigation of Signal Dependence on Diffusion Time. Novena Rangwala1, David Hackney1, David C. Alsop. 21st Annual Meeting and Exhibition, International Society of Magnetic Resonance in Medicine, Salt Lake City, UT, April, 2013.

Characterization of Diffusion Signal Decay in the Spinal Cord Based on Angular Dispersion of Axons. Novena Rangwala1, David Hackney1, David C. Alsop. 21st Annual Meeting and Exhibition, International Society of Magnetic Resonance in Medicine, Salt Lake City, UT, April, 2013.

CONCLUSION

This work has advanced imaging capabilities of normal and injured spinal cord. Principles have been validated in animal models and approaches have been implemented for human subjects.

REFERENCES

Wilhelm, M; Ong, H; Wehrli, S; Li, C; Ping-Huel, T; Hackney, D; Wehrli F. Direct magnetic resonance detection of myelin and prospects for quantitative imaging of myelin density. PNAS. 2012, 109, 24:9605-9610.

Rangwala, N; Hackney, DB; Dai, W; Alsop, D. Diffusion restriction in the human spinal cord characterized in vivo with high b-value STEAM diffusion imaging. Neuroimage. 2013. 82: 416-425.

APPENDICES

None